Renewable Energy 221 (2024) 119735

Contents lists available at ScienceDirect

Renewable Energy

journal homepage: www.elsevier.com/locate/renene

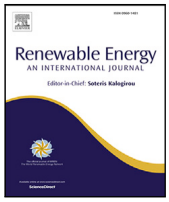

Enhanced Convolutional Neural Network for solar radiation nowcasting: All-Sky camera infrared images embedded with exogeneous parameters

Emanuele Ogliari [a,*], Maciej Sakwa [a], Paolo Cusa [b]

[a] Politecnico di Milano, via Lambruschini 4, Milan, 20156, Italy
[b] Enlight Energy Services S.R.L., Via Santa Maria Valle 3, Milan, 20123, Italy

ARTICLE INFO

MSC:
0000
1111

Keywords:
Nowcasting
Solar radiation forecast
All-Sky Images
Whole-Sky camera
Convolutional Neural Networks

ABSTRACT

Electrical power production by renewable energy sources is unpredictable in nature and this may cause imbalance between power generation and demand. Therefore, an accurate prediction of solar radiation is crucial for the stability and efficient management of electric grid. This study focuses on very short-term forecasts of solar radiation with a horizon in the range of 5–15 min. In this paper, a Convolutional Neural Network is proposed that uses sequences of infrared images captured by an All-Sky Imager to forecast the Global Horizontal Irradiance on different time horizon. A real case study, exploiting six months of high-resolution data, is analyzed. Additionally, an innovative technique, the Enhanced Convolutional Neural Network (ECNN), is proposed in which exogenous data, as the solar radiation measurement, is encoded in terms of colored pixels in the upper corner of the images. Considering the naïve persistence method as a baseline, a clear improvement across the key metrics has been noted with the proposed methodology. A deeper analysis of the results reveals that the proposed models are more accurate than persistence when high fluctuations of solar radiation are experienced. In that case, the ECNN achieves a forecast skill exceeding 19% for all the tested forecast horizons.

1. Introduction

The ever-increasing energy demand and the push towards a clean energy transition imposed by stronger environmental policies and ambitious climate targets lead to increased generation from renewable sources. In particular, solar photovoltaic energy (PV) is in the spotlight, and in 2021 it accounted for 60% of the worldwide annual renewable capacity additions [1]. Therefore, due to the intermittent and unpredictable nature of the solar source, the need for accurate solar radiation prediction is becoming crucial for grid connections and stand-alone networks.

This study focuses on very short-term forecasting, also known as nowcasting, to make predictions at three selected forecast horizons: 5, 10, and 15 min. The evaluation of solar radiation at such short timescales provides benefits for power smoothing processes, monitoring of real-time electricity dispatch, and PV storage control.

2. State-of-the-art solar nowcasting

Nowcasting has been identified as one of the main possible solutions to mitigate the unpredictable and variable nature of Renewable Energy Sources (RES) [2]. This task is particularly important in the balancing of Micro Grid (MG) systems and allows for better response to rapid ramp events and higher penetration of PV energy [3]. Compared to other solar technologies (such as solar thermal systems) PV energy generation is characterized by low inertia and swift response to sudden changes in weather conditions, resulting in increased significance of precise nowcasting. However, in recent years there has been ongoing research concerning implementations of solar nowcasting in installations based on solar thermal energy such as Concentrating Solar Thermal plants (CST) [4,5] where precise short-term forecasts are necessary for accurate demand planning of the dependent production units.

Nowcasting has lagged behind in research compared to longer forecast horizons. Nowadays, state-of-the-art is moving towards new technologies that are being developed to increase forecast reliability. Specifically, Convolutional Neural Networks (CNN) and thermal infrared All-Sky Imagers (ASI) are becoming useful tools to improve accuracy [6] as conventional statistics-based ML methods have already shown great potential [7].

Nowcasting has proven to be successful in predictions of weather conditions through numerical methods and satellite images [8], or RGB and IR camera imaging [9] that has been successfully related

* Corresponding author.
E-mail address: emanuelegiovanni.ogliari@polimi.it (E. Ogliari).

https://doi.org/10.1016/j.renene.2023.119735
Received 31 July 2023; Received in revised form 29 October 2023; Accepted 23 November 2023
Available online 24 November 2023

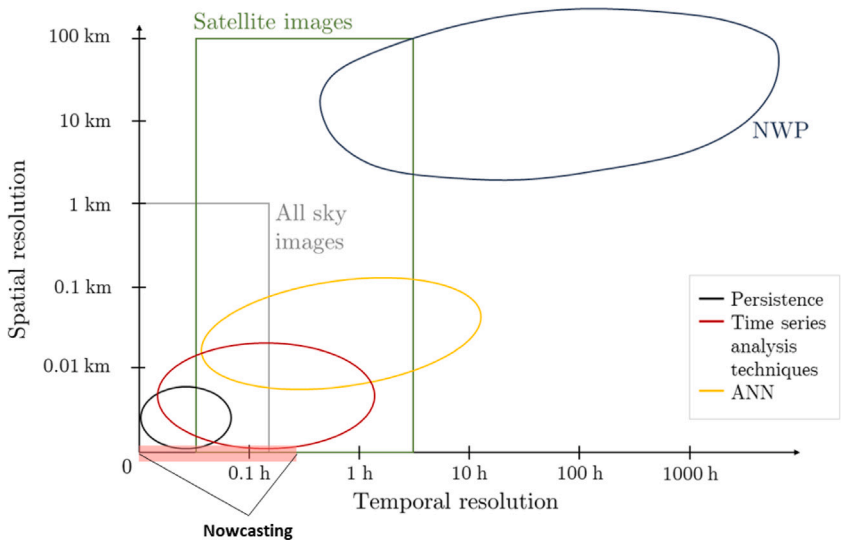

Fig. 1. Model classification based on temporal and spatial resolutions.

to PV production predictions through solar radiation prediction [10]. However, in highly polluted environments, it is significantly more difficult with examples showing nonlinear behavior [11].

ASI allows for high-precision nowcasting in comparison to weather-based predictions, with a visible correlation between ASI sky-image features and the power output of a PV panel [12]. In particular, good results are obtained when a network of sensors is used [13]. ASI-based predictions are often related to short-term forecasts of weather conditions in the location of the PV power plant. Applications studied already include solar position identification [14], cloud cover and sky-clearness nowcasting [15,16], estimations of cloud height [17], and general cloud movement and velocity predictions [18]. Usually on the technical side, the forecasting is powered by Machine Learning [19], such as CNN with good accuracy obtained already [20,21] with IR imaging outperforming visible range [22]. The targets for network training are usually defined with reference to the Perez–Ineichen clear sky model [23,24].

Nowcasting and short-term forecasts are also becoming widely used in other weather-dependent RES, such as wind power [25]. Short-term forecasts with a few-hour horizon have been performed with good results [26], with the research now moving to sub-hourly predictions [27,28] even with highly variable wind fields with the use of deep learning [29]. In the forecasting field, the most popular one is persistence, which belongs to the larger class of naïve methods. Despite their simplicity, which leads both to low computational and time costs, they are surprisingly effective and considered sufficiently accurate for very short-term forecasting. Fig. 1 shows the most adopted technique for solar forecasting based on temporal and spatial resolution.

3. Motivations and research questions

The main goal of the research is to provide a forecasting technique for the immediate future based on promising state-of-the-art technologies: CNNs and infrared ASI. For short-term predictions, these methods are usually fairly accurate however they often struggle to outperform persistence which is a naïve but generally reliable method [6]. In particular, the persistence method is unbeatable in terms of complexity and computational burden.

To improve the performance of the CNN-based methodology, we propose in this paper an innovative technique in which exogenous data about the state corresponding to the ASI picture is encoded as information directly in the images. This should allow the model to perform better in unclear conditions and distinguish easily between sunny and fully overcast conditions. The newly designed methodology will be referred to as an Enhanced Convolutional Neural Network (ECNN) and will be thoroughly compared to other models such as CNN and persistence.

4. Data acquisition

The dataset was collected from a thermal infrared all-sky imager and a meteorological station both located in Milan, at the SolarTech^{LAB} of the Politecnico di Milano (latitude: 45.50°N; longitude: 9.16°E). Infrared all-sky images and numerical meteorological measurements were collected in the period between 18th September 2019 and 9th April 2020, with an interruption period of recording between 23th December 2019 and 12th February 2020.

Images were taken with a time resolution of 1 min resulting in a total number equal to 116,891.

4.1. Thermal infrared all sky imager

The Thermal Infrared All Sky Imager used is the Sky InSight^{TM} developed by Reuniwatt. It includes a long-wavelength infrared camera that takes a picture with a 640 × 480 spatial resolution every 60 s. The imager is mounted on a mast to film a hemispherical mirror pointing at the sky, which provides a 180° field of view.

Infrared radiation has broad prospects for providing valuable atmospheric properties. In fact, the spectral emission of sky which ranges from 8 to 13 μm is very sensitive to water vapor presence, facilitating the identification of clouds. The main advantages of infrared pictures compared to visible images are better overall cloud features as well as the absence of Sun glare effect in Sun-region [30]. Fig. 2(a) and (b) show the significant difference between the two images taken at the same time.

There is however an innegligible drawback related to overcast weather. Under those conditions, the clouds cover the entire sky and the infrared camera interprets the sky dome as having an approximately equal temperature everywhere. This means that there is no possibility to distinguish sky and clouds as in the case of partly cloudy weather from the IR picture itself. Fig. 3(a) and (b) show the similarity between clear and overcast skies.

4.2. Meteorological station

The environmental data were collected at a weather station located at the Department of Energy of Politecnico di Milano (latitude:

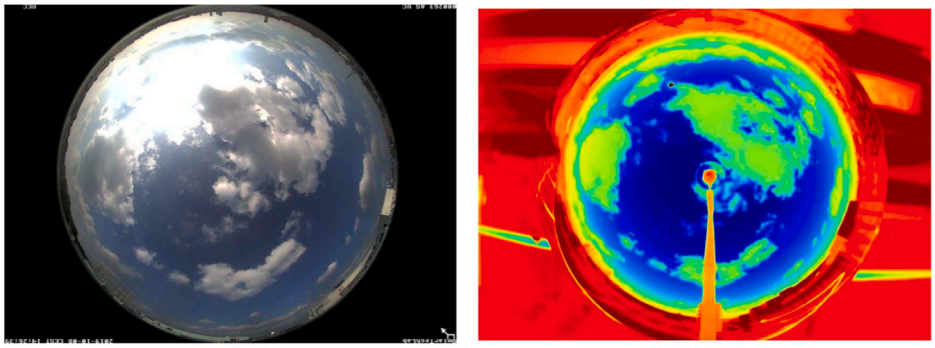

(a) (b)

Fig. 2. Camera images: (a) visible spectrum, (b) IR spectrum.

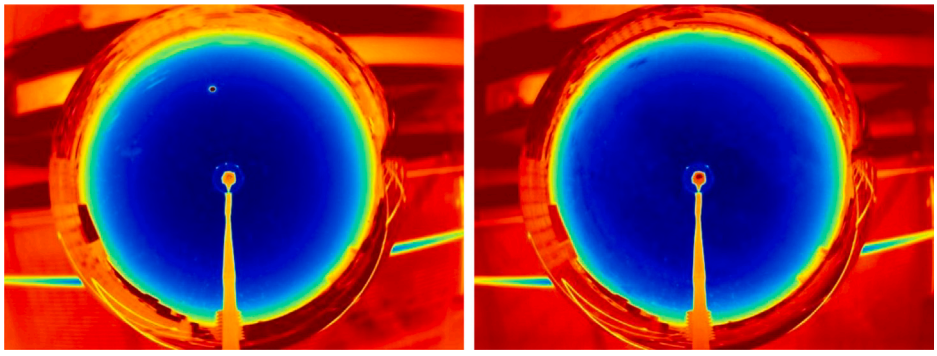

(a) (b)

Fig. 3. IR camera images: (a) sunny day, (b) overcast day.

45.50°N; longitude: 9.16°E). It is equipped with solar irradiance sensors, temperature and humidity sensors, a wind speed and direction sensor, and a rain collector. Irradiance was measured with two secondary standard pyranometers, which evaluate the global irradiance on the horizontal and 30° tilted planes. Measurements were performed every ten seconds. The average, maximum, minimum, and standard deviation of the values measured were calculated every minute.

5. Proposed methodology

The proposed nowcasting technique is based on a CNN where a sequence of three consecutive images is used as an input feature space. As a result, the CNN has the ability to detect the movement of the clouds and predict its impact on the irradiance in the following minutes.

However, before the training and testing of the network may begin the available image dataset has to be pre-processed to obtain better results both in terms of performance and execution time.

5.1. Pre-processing

In the initial step, the images are filtered to remove instances when unclear weather conditions could highly impact the forecast accuracy. Firstly, all the images where precipitation was recorded have been removed (as rain has a significant negative impact on the quality of images). Moreover, clear sky thermal radiance increases with air mass (see Fig. 4), and at sunrise and sunset, the region of the sky around the Sun is limited due to the presence of land. For this reason, the detection of clouds is particularly hard in that area. Hence, images characterized by a Sun elevation angle lower than 20° were also not considered by the forecasting model. The filtering results in a reduction of the total number of images available to the neural network to 33,686 (from the starting 116,891) as no additional data augmentation techniques are used.

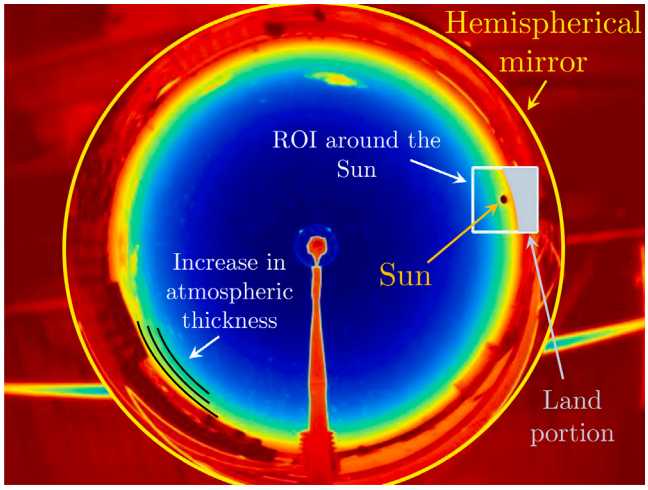

Fig. 4. Infrared image and its characteristics. The color changes near the horizon due to the increase in atmospheric thickness. A limited portion of the sky in the Region of Interest (ROI) around the Sun is visible at a low Sun elevation angle.

In the second step, the images are flattened from three channels (Red–Green–Blue format) to one channel (grayscale) with the goal of accelerating the training process since the amount of image data is reduced. To replicate the color scale of the original image the 'Jet' function implemented in Matlab was used. Each RGB pixel value was compared with the jet function to find the nearest correspondence. Its

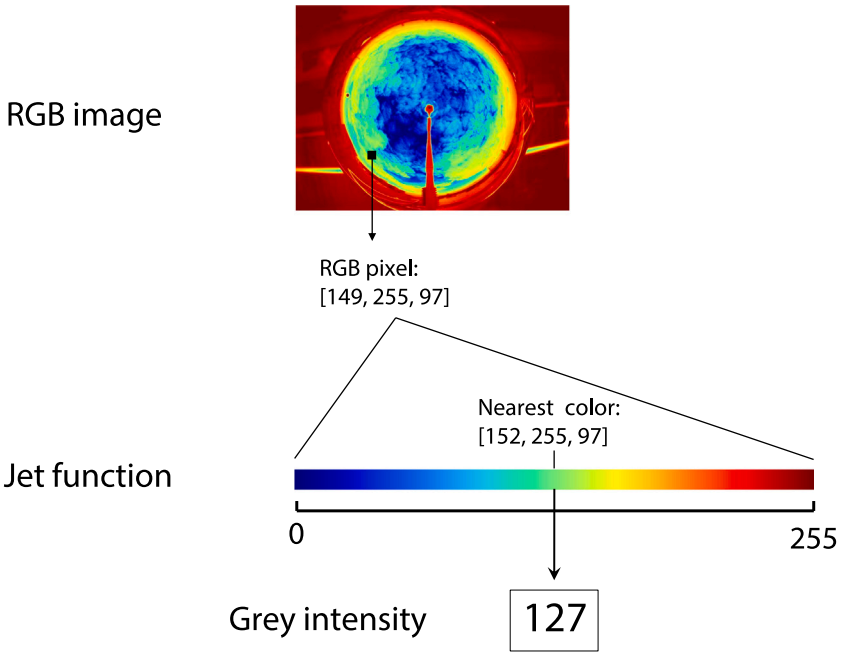

Fig. 5. Illustration of the image transformation process from RGB to grayscale.

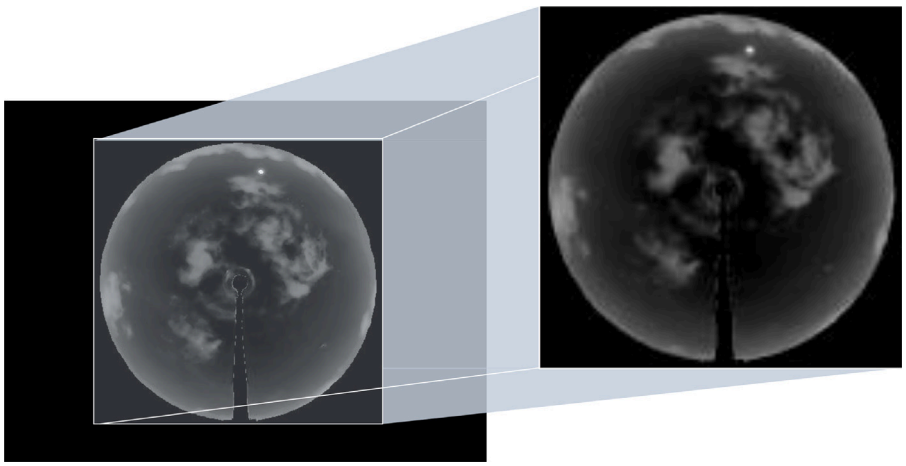

Fig. 6. Cropping and scaling.

index represents the gray intensity value of the monochrome image. The entire process is depicted in Fig. 5.

The second step is concluded by the application of a mask to remove all parts that are not the sky. Finally, the images are cropped. A square area of 384 × 384 pixels size is cut out from the original picture and scaling is performed to reduce the image size to a third in each direction (as in Fig. 6). In this way, unnecessary data is removed and we end up with a final image of 128 × 128 pixels.

5.2. CNN architecture

Fig. 7 depicts the architecture of the used CNN that is inspired by the one developed by the Visual Geometry Group (VGG) [31]. This structure is well-researched and widely used due to its good performance at image classification and low complexity. It consists of five Feature Learning Blocks (FLBs). Each FLB consists of two or three convolutional layers with the same parameters and a max-pooling layer. The first FLB has layers with 64 filters, whereas the second has 128 filters, the third 256 filters, and the fourth and the fifth 512 filters accordingly. All layers use the same kernel size (3 × 3) and Same padding. This configuration has resulted in optimal results in extensive tests. After the convolution part, there are two linear fully-connected layers. The first one has 256 neurons and the second has 1 neuron. This last neuron is responsible for providing the predicted value. The ReLU activation function was used in convolutional layers, whereas the linear activation function was used in fully-connected layers. Lastly, a 0.2 dropout was put before each linear layer to avoid overfitting. The model was trained with an initial learning rate of 0.0001 with the Adam optimizer and the loss function adopted was the Mean Absolute Error.

5.3. Enhanced convolutional neural network

The ECNN is created by adding exogenous data information to the images used by CNN with the goal of improving forecasting performance without changing the structure of the deep learning model. Hence, there is no added complexity to the network itself, but rather an additional data transformation step in the image pre-processing pipeline.

Exogenous data is codified into pixels and placed horizontally in the upper left corner of the image that does not obstruct the sky region.

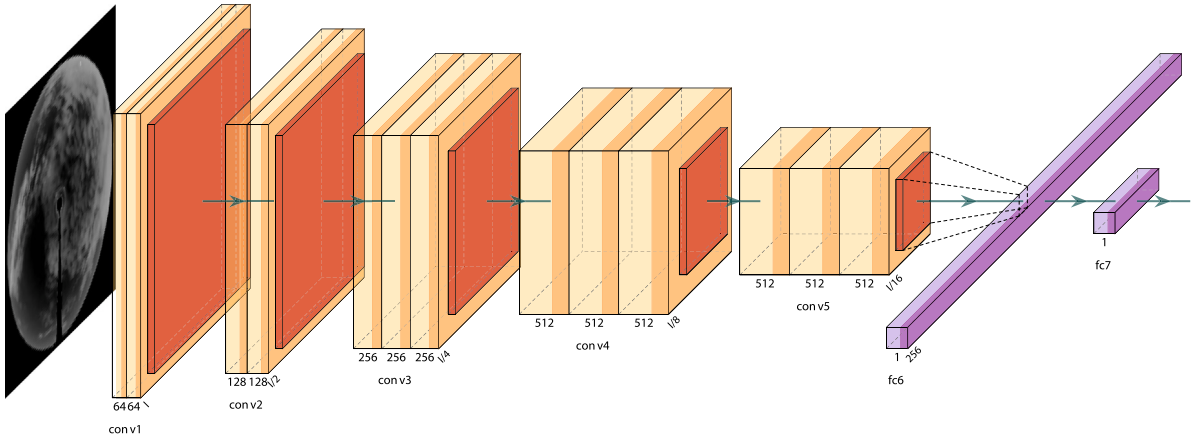

Fig. 7. CNN architecture.

Fig. 8. Codified exogenous data.

More specifically, the inserted data is Global Horizontal Irradiation (GHI) measured at the exact time of the image acquisition. In particular, the overall sum of the modified pixels is equal to the measured GHI, as shown in Fig. 8, where the maximum value of a grayscale 8-bit pixel is 255 (2^8-1). The encoded GHI is in fact closely related to the prediction target which is based on the value of the solar radiation measured within the selected forecast horizon.

5.4. Sequence generation

To ensure proper data structure and incentivize learning of the intrinsic temporal patterns within the data, the images are processed together in sequences of three. A unique sequence is generated for each of the 33,686 images by concatenating them along the channel dimension as depicted in Fig. 9. Hence, assuming that three images are concatenated as the input of the forecasting model, the input has the size of $H \times W \times (3 \cdot C)$. Where H and W is the image's height and width and C is the number of channels (in this case equal to 1). Depending on the selected forecast horizon (Δt_{pred}) an adequate time interval (Δt_{back}) has to be chosen between the sequenced images and is by default close to half of the forecast horizon. It is equal to 2', 4' and 8' for Δt_{pred} equal to 5', 10', and 15' respectively. This input concatenation operation is described in Eq. (1).

$$I_{input} = (I_{t-2\Delta t_{back}} \oplus I_{t-\Delta t_{back}} \oplus I_t) \tag{1}$$

In the equation, the symbol $\oplus$ indicates the concatenation between images (I), t is the actual time, and Δt_{back} is the selected time interval between images in the sequence.

The created sequences are later shuffled in order to improve the model generalization performance. The resulting sequence dataset is later split into: *training*, *validation* and *test* subsets with sizes of 64%, 16%, and 20% respectively.

5.5. Training labels

The movement of the clouds that can be extrapolated from the sequences is subsequently correlated with the GHI through the given training labels. In reality, the model does not directly predict the GHI, but the GHI is normalized by the Clear Sky Global Horizontal Irradiance (GHI_{cs}). This last term is computed through the Ineichen and Perez clear sky model which can be simulated in the PVlib Python package [32]. The resulting parameter is called the Clear Sky Index (CSI) and it is a dimensionless parameter that directly informs on the weather conditions. For most cases, the value of this parameter ranges between 0 and 1. Each sequence of images is associated with a label defined at the selected forecast horizon. In other words, the target corresponds to the CSI value measured by waiting for a period corresponding to the forecast horizon from the last image in the chronological order of the sequence. Considering a sequence of three images taken at t, t-Δt_{back} and t-$2\Delta t_{back}$, the CSI for that sequence is measured at t+Δt_{pred}.

An early stopping procedure is implemented during training to avoid model overfitting.

6. Banchmarks and evaluation metrics

Two models were used as a baseline for the ML model test. First, the dataset of forecasts computed in 2020 by a weather broadcaster provider, that similarly exploited the infrared images and the GHI measurements collected by the meteorological station at the SolarTech^{LAB}. Second, a naïve persistence method which assumes a constant CSI within the forecast horizon, resulting in a time-shift of the GHI curve.

For the evaluation of the model, three indexes are selected: the *Root Mean Squared Error* (RMSE) [33], the *Mean Bias Error* (MBE) [34], and the *Forecast Skill* (FS) [35] that are defined as:

$$RMSE = \sqrt{\frac{1}{N}\sum_{i=1}^{N}(y_{\text{pred}} - y_{\text{meas}})^2} \quad (W/m^2) \tag{2}$$

$$MBE = \frac{1}{N}\sum_{i=1}^{N}(y_{\text{pred}} - y_{\text{meas}}) \quad (W/m^2) \tag{3}$$

$$FS = 1 - \frac{RMSE}{RMSE_p} \quad (-) \tag{4}$$

The results were obtained using an NVIDIA®T4 GPU on Google Colaboratory. with an average run time of the simulations of less than two hours.

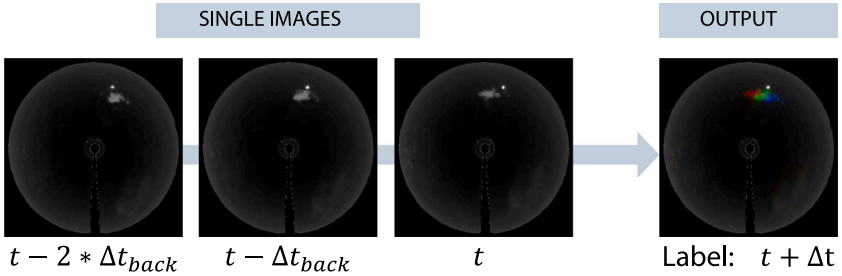

Fig. 9. Sequence of images.

Table 1
Detailed results (RMSE, MBE, FS) for the tested models and forecast horizons.

	Horizon	Persistence	Weather broad.	CNN	ECNN
RMSE	5 min	63.47	90.57	74.88	60.26
	10 min	76.66	86.99	77.46	69.32
	15 min	88.18	91.46	87.82	80.18
MBE	5 min	−0.4	−8.3	20.70	3.90
	10 min	−1.12	−6.59	13.48	9.42
	15 min	−2.59	−8.59	1.05	16.47
FS	5 min	0	−40.74	−17.97	5.05
	10 min	0	−17.82	−32.44	9.57
	15 min	0	−3.72	0.41	9.07

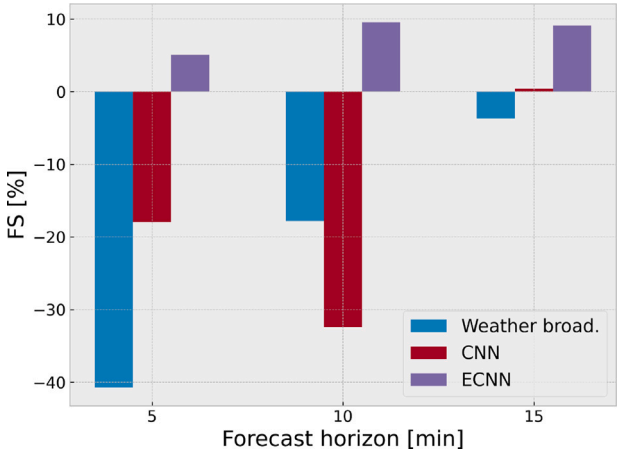

Fig. 10. Forecast Skill (referred to persistence) of the tested methods.

7. Results and discussion

The RMSE, MBE, and FS were computed as functions of the forecast horizons and the historical timestep. These metrics were then compared among the predictions provided by the weather broadcaster and CNN method. The detailed results can be seen in Table 1.

The results show how the CNN model is able to outperform the predictions of the meteorological provider for all forecast horizons. Moreover, the proposed method matches the persistence method, except for predictions 5 min ahead due to the high accuracy of persistence at those timescales. The ECNN instead always outperforms persistence with FS of 5.05%, 9.57%, and 9.07% for 5', 10', and 15' respectively. These results are depicted in Fig. 10.

Looking at the CNN models that got the best FS, they follow the real curve with good accuracy, but they hardly ever outperform persistence. In particular, the CNN tends to behave like a *smart* persistence model, avoiding large errors at the expense of missing peaks and having regular time delays. This behavior is evident in Fig. 11, in which all the ramps are missed, but both CNN and ECNN got FS higher than 14%.

Fig. 12 on the other hand shows that the main problem of the proposed method is the overcast days. Here, the CNN models have errors at least three times larger than those observed with persistence. In overcast, the weather conditions are hard to evaluate by the CNN for two main reasons: first, the impossibility of the CNN to know the Sun position; second, the similarity, in infrared images, between cloudy days and clear sky (as shown before on Fig. 3). The result is a high positive bias present in all the analyses.

Fig. 13 presents the performance of the model in clear sky conditions. As can be seen, despite close matching between the prediction line and the true GHI values (especially in the afternoon) the model is not able to outperform the persistence. However, the model becomes more reliable with an increased forecast horizon as the persistence results begin to deviate further from the recorded sensor values.

7.1. Analysis on high fluctuations of irradiance

Usually, results provided by the forecasting models are strictly dependent on the experienced meteorological conditions. Specifically, they incur larger errors on partially cloudy days due to the greater variation of GHI compared to clear-sky days. However, here the models are analyzed from a different perspective by looking at the instances characterized by high fluctuations in solar irradiance. Probability Density Functions (PDF) of the change between the current GHI and the future value were generated for a chosen partially cloudy day. Considering that the choice of the forecast horizon impacts the GHI variation, we end up with three PDFs for 5, 10, and 15 min ahead. The curves reported in Fig. 14 show that most of the irradiance variations are relatively small (lower than 60 W/m^2). However, the high fluctuations (marked in red on the graphs) are fundamental for both electric grid balancing and microgrid management. Focusing on these aspects, models can be evaluated in terms of FS under conditions that rarely occur but are still statistically significant. In particular, at least 80% of the most probable data (marked in light blue on the graphs) were removed and not considered by the new error metrics.

The results for CNN and ECNN are presented in Fig. 15. Here, a clear and significant benefit of implementing the CNN models can be observed with FS values always higher than 19% for all the forecast horizons.

This analysis demonstrates the factual added value that neural networks can bring to the nowcasting field. The CNN (and the ECNN) could significantly boost the performance of prediction when high variability of data is considered. Well-trained neural networks, can adapt to changes in the environment quicker then persistence and numerical methods. It means that a new criterion can be applied to the forecasting analysis. A proper prediction model can be chosen depending on how far the recorded instances stray from the expected value.

Most of the previous results highlight that persistence is still mostly unbeatable method in very short-term (5') predictions, especially considering its negligible computational load. As for the neural network, the obvious solution to improve the FS of CNN-based methods is to provide more information (either in the form of raw data or other exogenous parameters) to the model at the expense of an even-increased computational burden. As an example, the exogenous data could be at

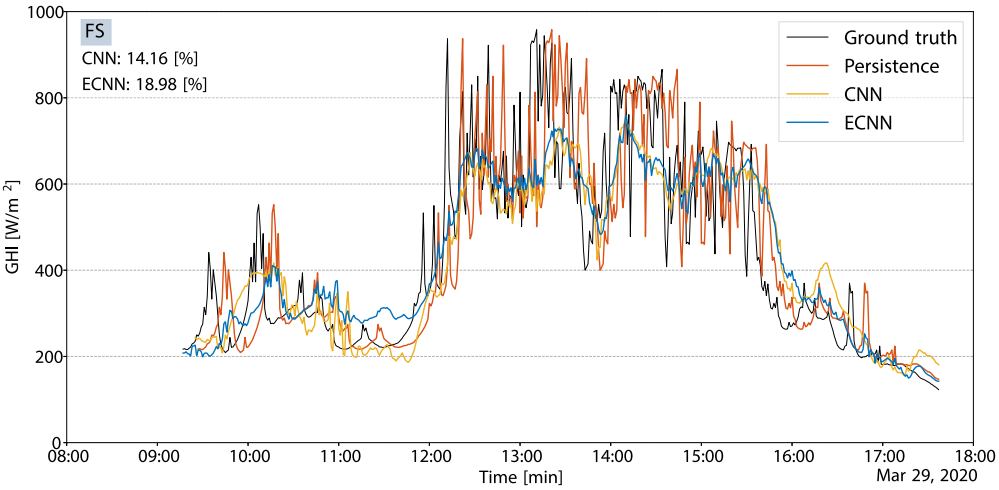

Fig. 11. 29th March 2020 – partly cloudy – 10 min forecast horizon.

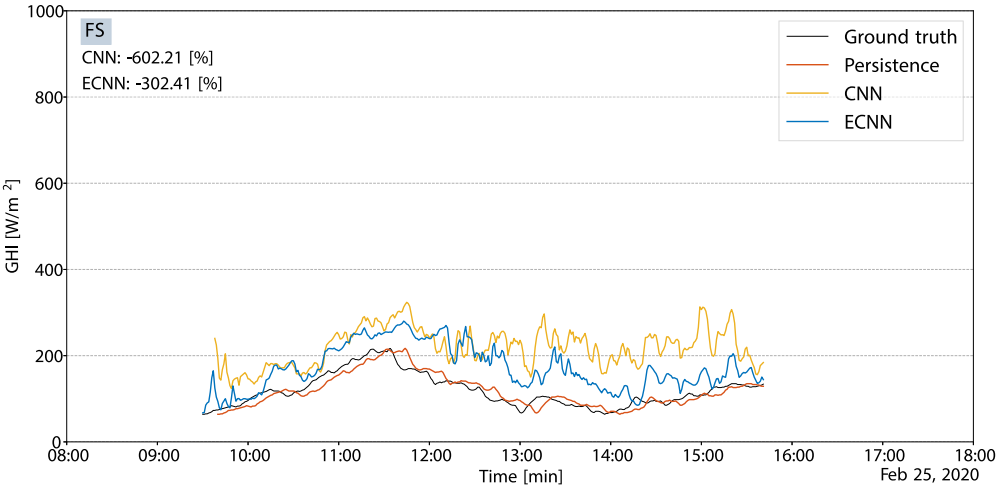

Fig. 12. 25th February 2020 – overcast – 10 min forecast horizon.

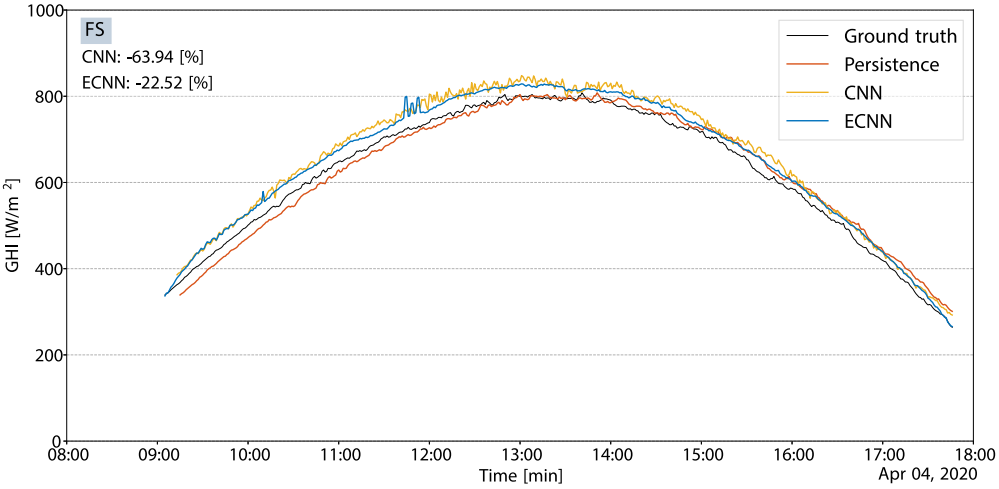

Fig. 13. 4th April 2020 – clear sky – 10 min forecast horizon.

a later stage decoded by the model and used as an auxiliary input to the final linear layers that perform the regression operation.

Moreover, despite the RMSE and the FS indicating a better performance of CNN compared to persistence (which is further amplified in case of high fluctuations of irradiance), the GHI curves reveal the tendency of both the CNN methods to operate conservatively, favoring a smoothing trend in the predictions concerning forecast ramps. This last aspect suggests the need for additional metrics of forecast evaluation,

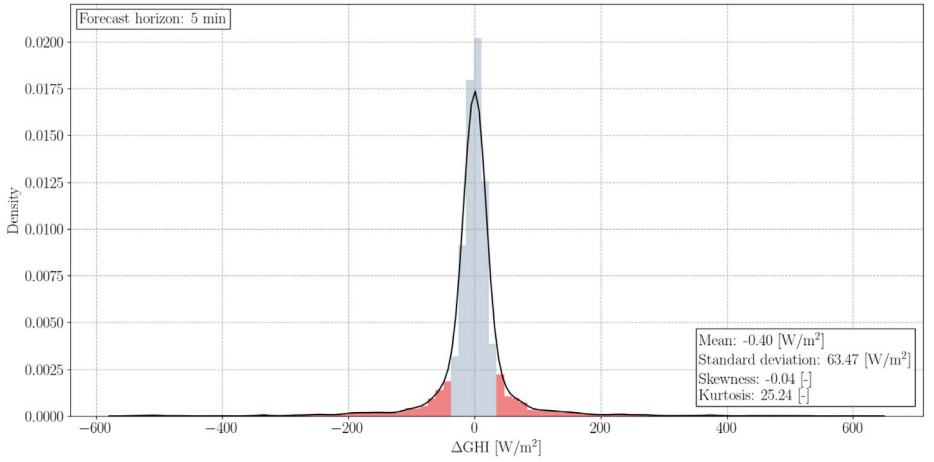

(a)

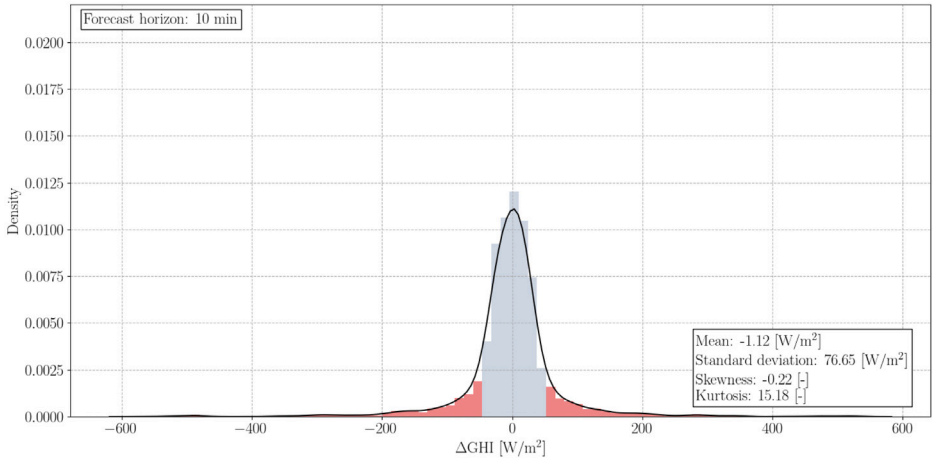

(b)

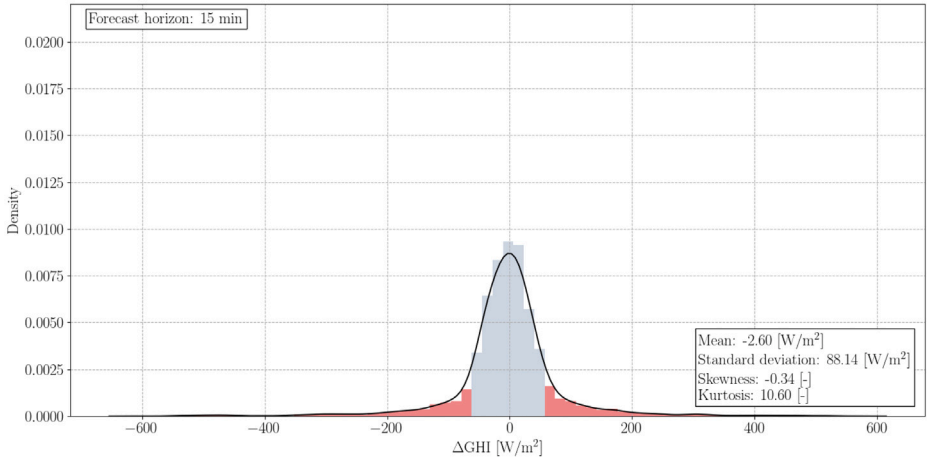

(c)

Fig. 14. Probability density functions for (a) 5 min, (b) 10 min (c) 15 min forecast.

which could measure the forecast delay or the ability to predict peaks and drops [36].

In general, these results are in line with other research ongoing in this area, with ML-based methodologies outperforming persistence. For example, in [36] the authors achieved a maximum FS of 20.4% by utilizing a ConvLSTM prediction model. However, their implementation was based on visible spectrum images and employed a longer sequence as the model input. In [37] the same authors boost the overall model performance to over 23% by combining the ASI with satellite image data. In addition to better results, this allowed to improve the model's performance in overcast conditions, as satellite images give a clear idea on whether the sky is actually covered or clear. Nonetheless, in clear-sky conditions, the model is similarly consistently outperformed by the naïve persistence methods.

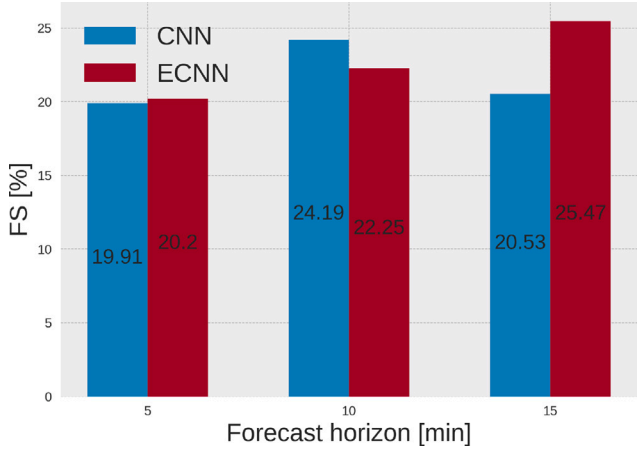

Fig. 15. Forecast Skill in fluctuating conditions.

8. Conclusion

In this work, we developed a CNN for the very short-term forecasting of solar radiation on the horizontal plane. The inputs are composed of a dataset of infrared sky images, measurements of the global horizontal irradiance, and the Ineichen and Perez clear sky model. The CNN method stacked three grayscale images with a 128 × 128 resolution to detect the dynamics of the clouds' motion. Furthermore, an innovative forecasting technique has been proposed: the Enhanced Convolutional Neural Network (ECNN).

The ECNN method outperforms all the considered benchmark models in the examined time horizons and it is more accurate than persistence: positive forecast skill scores of 5.04%, 9.57%, and 9.07% were obtained for 5, 10, and 15 min ahead respectively.

The work made use of RGB pictures (instead of raw grayscale), with colormap designed to maximize the contrast under any conditions for better recognition by human eyes. However, this results in a similarity between overcast and clear sky conditions, which negatively affects the performance of the model on overcast days. A significant forecast improvement can be found with the computation of more elaborated cloud products. Sky InSight can be used to compute the Cloud Optical Depth, which is a valuable parameter for knowing the clouds' properties and characteristics [30]. Lastly, an analysis of periods characterized by high fluctuations of irradiance was carried out since they are the most crucial from the perspective of microgrid management. The results show a significant improvement in the proposed method with respect to persistence, which reaches an FS score higher than 19.9%.

CRediT authorship contribution statement

Emanuele Ogliari: Conceptualization, Methodology, Supervision. **Maciej Sakwa:** Data curation, Writing – original draft, Software, Validation. **Paolo Cusa:** Visualization, Investigation, Writing – review & editing.

Declaration of competing interest

The authors declare that they have no known competing financial interests or personal relationships that could have appeared to influence the work reported in this paper.

Acknowledgment

We thank Reuniwatt for providing the infrared all-sky imager Sky InSight and data used in this study to observe and analyze the cloud cover. This study was partly conducted within the Agritech National Research Center and received partial funding from the European Union Next-GenerationEU (PIANO NAZIONALE DI RIPRESA E RESILIENZA (PNRR) – MISSIONE 4 COMPONENTE 2, INVESTIMENTO 1.4 – D.D. 1032 17/06/2022, CN00000022). This manuscript reflects only the authors' views and opinions, neither the European Union nor the European Commission can be considered responsible for them.

References

[1] IEA, Renewables 2021 - Analysis and forecast to 2026, 2021, URL www.iea.org.
[2] S.R. Sinsel, R.L. Riemke, V.H. Hoffmann, Challenges and solution technologies for the integration of variable renewable energy sources—A review, Renew. Energy 145 (2020) 2271–2285, http://dx.doi.org/10.1016/j.renene.2019.06.147.
[3] R. Samu, M. Calais, G. Shafiullah, M. Moghbel, M.A. Shoeb, C. Carter, Advantages and barriers of applying solar nowcasting in controlling microgrids: Findings from a survey in 2020, in: 2020 International Conference on Smart Grids and Energy Systems, SGES, 2020, pp. 267–272, http://dx.doi.org/10.1109/SGES51519.2020.00054.
[4] L. Ramírez, J. Vindel, Forecasting and nowcasting of DNI for concentrating solar thermal systems, Adv. Concentrating Solar Therm. Res. Technol. (2017) 293–310.
[5] S.C. Rowe, I. Hischier, A.W. Palumbo, B.A. Chubukov, M.A. Wallace, R. Viger, A. Lewandowski, D.E. Clough, A.W. Weimer, Nowcasting, predictive control, and feedback control for temperature regulation in a novel hybrid solar-electric reactor for continuous solar-thermal chemical processing, Sol. Energy 174 (2018) 474–488.
[6] S.-A. Logothetis, V. Salamalikis, S. Wilbert, J. Remund, L.F. Zarzalejo, Y. Xie, B. Nouri, E. Ntavelis, J. Nou, N. Hendrikx, L. Visser, M. Sengupta, M. Pó, R. Chauvin, S. Grieu, N. Blum, W. van Sark, A. Kazantzidis, Benchmarking of solar irradiance nowcast performance derived from all-sky imagers, Renew. Energy 199 (2022) 246–261, http://dx.doi.org/10.1016/j.renene.2022.08.127.
[7] X. Chen, Y. Du, E. Lim, L. Fang, K. Yan, Towards the applicability of solar nowcasting: A practice on predictive PV power ramp-rate control, Renew. Energy 195 (2022) 147–166, http://dx.doi.org/10.1016/j.renene.2022.05.166.
[8] A. Catalina, C.M. Alaíz, J.R. Dorronsoro, Combining numerical weather predictions and satellite data for PV energy nowcasting, IEEE Trans. Sustain. Energy 11 (3) (2020) 1930–1937, http://dx.doi.org/10.1109/TSTE.2019.2946621.
[9] E. Nueve, R. Jackson, R. Sankaran, N. Ferrier, S. Collis, WeatherNet: Nowcasting net radiation at the edge, in: 2021 IEEE Conference on Technologies for Sustainability, SusTech, 2021, pp. 1–7, http://dx.doi.org/10.1109/SusTech51236.2021.9467444.
[10] J. Heo, K. Song, S. Han, D.-E. Lee, Multi-channel convolutional neural network for integration of meteorological and geographical features in solar power forecasting, Appl. Energy 295 (2021) 117083.
[11] D. Jia, L. Yang, T. Lv, W. Liu, X. Gao, J. Zhou, Evaluation of machine learning models for predicting daily global and diffuse solar radiation under different weather/pollution conditions, Renew. Energy 187 (2022) 896–906, http://dx.doi.org/10.1016/j.renene.2022.02.002.
[12] R. Zhang, H. Ma, T.K. Saha, X. Zhou, On sky imaging analysis and deep learning for photovoltaic output nowcasting, in: 2020 IEEE Power & Energy Society General Meeting, PESGM, 2020, pp. 1–5, http://dx.doi.org/10.1109/PESGM41954.2020.9281668.
[13] T. Schmidt, J. Stührenberg, N. Blum, J. Lezaca, A. Hammer, T. Vogt, A network of all sky imagers (ASI) enabling accurate and high-resolution very short-term forecasts of solar irradiance, in: 21st Wind & Solar Integration Workshop, Vol. 2022, WIW 2022, 2022, pp. 372–378, http://dx.doi.org/10.1049/icp.2022.2778.
[14] A. Nespoli, A. Niccolai, Solar position identification on sky images for photovoltaic nowcasting applications, in: 2020 IEEE International Conference on Environment and Electrical Engineering and 2020 IEEE Industrial and Commercial Power Systems Europe, EEEIC / I&CPS Europe, 2020, pp. 1–5, http://dx.doi.org/10.1109/EEEIC/ICPSEurope49358.2020.9160490.
[15] L. Berthomier, B. Pradel, L. Perez, Cloud cover nowcasting with deep learning, in: 2020 Tenth International Conference on Image Processing Theory, Tools and Applications, IPTA, 2020, pp. 1–6, http://dx.doi.org/10.1109/IPTA50016.2020.9286606.
[16] X. Zhao, H. Wei, H. Wang, T. Zhu, K. Zhang, 3D-CNN-based feature extraction of ground-based cloud images for direct normal irradiance prediction, Sol. Energy 181 (2019) 510–518, http://dx.doi.org/10.1016/j.solener.2019.01.096.
[17] E. Ogliari, A. Nespoli, E. Collino, D. Ronzio, Cloud-base height estimation based on CNN and all sky images, Eng. Proc. 18 (1) (2022) 5.
[18] M. Caldas, R. Alonso-Suárez, Very short-term solar irradiance forecast using all-sky imaging and real-time irradiance measurements, Renew. Energy 143 (2019) 1643–1658.

[19] M. Trigo-González, M. Cortés-Carmona, A. Marzo, J. Alonso-Montesinos, M. Martínez-Durbán, G. López, C. Portillo, F.J. Batlles, Photovoltaic power electricity generation nowcasting combining sky camera images and learning supervised algorithms in the Southern Spain, Renew. Energy 206 (2023) 251–262, http://dx.doi.org/10.1016/j.renene.2023.01.111.

[20] Y. Sun, G. Szucs, A.R. Brandt, Solar PV output prediction from video streams using convolutional neural networks, Energy Environ. Sci. 11 (2018) 1811–1818, http://dx.doi.org/10.1039/c7ee03420b.

[21] O. Liandrat, A. Braun, E. Buessler, M. Lafuma, S. Cros, A. Gomez, L.-E. Boudreault, Sky-imager forecasting for improved management of a hybrid photovoltaic-diesel system, in: Proc. 3rd International Hybrid Power Systems Workshop, 2018.

[22] G. Terrén-Serrano, M. Martínez-Ramón, Comparative analysis of methods for cloud segmentation in ground-based infrared images, Renew. Energy 175 (2021) 1025–1040.

[23] D. Pothineni, M.R. Oswald, J. Poland, M. Pollefeys, KloudNet: Deep learning for sky image analysis and irradiance forecasting, in: T. Brox, A. Bruhn, M. Fritz (Eds.), Pattern Recognition, Springer International Publishing, Cham, 2019, pp. 535–551.

[24] R. Perez, P. Ineichen, K. Moore, M. Kmiecik, C. Chain, R. George, F. Vignola, A new operational model for satellite-derived irradiances: description and validation, Sol. Energy 73 (5) (2002) 307–317.

[25] D. Bouche, R. Flamary, F. d'Alché Buc, R. Plougonven, M. Clausel, J. Badosa, P. Drobinski, Wind power predictions from nowcasts to 4-hour forecasts: A learning approach with variable selection, Renew. Energy 211 (2023) 938–947, http://dx.doi.org/10.1016/j.renene.2023.05.005.

[26] H. Wang, J. Yan, S. Han, Y. Liu, Switching strategy of the low wind speed wind turbine based on real-time wind process prediction for the integration of wind power and EVs, Renew. Energy 157 (2020) 256–272, http://dx.doi.org/10.1016/j.renene.2020.04.132.

[27] A. Dupré, P. Drobinski, B. Alonzo, J. Badosa, C. Briard, R. Plougonven, Sub-hourly forecasting of wind speed and wind energy, Renew. Energy 145 (2020) 2373–2379, http://dx.doi.org/10.1016/j.renene.2019.07.161.

[28] M. Contu, R. Gnudi, F. Allella, A. Pascucci, E.M. Carlini, A.C. Murgia, P.L. Marongiu, E. Carcassi, I. Andriyets, E. Ghiani, F. Pilo, Wind power forecasting models for very short-term operation of power systems, in: 2021 AEIT International Annual Conference, AEIT, 2021, pp. 1–6, http://dx.doi.org/10.23919/AEIT53387.2021.9627018.

[29] H. Gao, C. Shen, Y. Zhou, X. Wang, P.-W. Chan, K.-K. Hon, J. Li, A deep learning-based wind field nowcasting method with extra attention on highly variable events, IEEE Geosci. Remote Sens. Lett. 19 (2022) 1–5, http://dx.doi.org/10.1109/LGRS.2022.3212904.

[30] C. Bertin, S. Cros, L. Saint-Antonin, N. Schmutz, Prediction of optical communication link availability: Real-time observation of cloud patterns using a ground-based thermal infrared camera, 9641, SPIE, 2015, p. 96410A, http://dx.doi.org/10.1117/12.2194920,

[31] K. Simonyan, A. Zisserman, Very deep convolutional networks for large-scale image recognition, 2014, arXiv preprint arXiv:1409.1556.

[32] W.F. Holmgren, C.W. Hansen, M.A. Mikofski, Pvlib Python: A Python package for modeling solar energy systems, J. Open Source Softw. 3 (29) (2018) 884.

[33] R.J. Hyndman, A.B. Koehler, Another look at measures of forecast accuracy, Int. J. Forecast. 22 (4) (2006) 679–688, http://dx.doi.org/10.1016/j.ijforecast.2006.03.001.

[34] B. Urquhart, M. Ghonima, D.A. Nguyen, B. Kurtz, C.W. Chow, J. Kleissl, Chapter 9 - sky-imaging systems for short-term forecasting, in: J. Kleissl (Ed.), Solar Energy Forecasting and Resource Assessment, Academic Press, Boston, 2013, pp. 195–232, http://dx.doi.org/10.1016/B978-0-12-397177-7.00009-7.

[35] Glossary of Meteorology, Skill, Tech. Rep., American Meteorological Society, 2023, URL http://glossary.ametsoc.org/wiki/climatology.

[36] Q. Paletta, G. Arbod, J. Lasenby, Benchmarking of deep learning irradiance forecasting models from sky images–An in-depth analysis, Sol. Energy 224 (2021) 855–867.

[37] Q. Paletta, G. Arbod, J. Lasenby, Omnivision forecasting: Combining satellite and sky images for improved deterministic and probabilistic intra-hour solar energy predictions, Appl. Energy 336 (2023) 120818, http://dx.doi.org/10.1016/j.apenergy.2023.120818.